Carbon 196 (2022) 10–19

Contents lists available at ScienceDirect

Carbon

journal homepage: www.elsevier.com/locate/carbon

Volumetric incorporation of NV diamond emitters in nanostructured F2 glass magneto-optical fiber probes

Adam Filipkowski [a,b], Mariusz Mrózek [c], Grzegorz Stępniewski [a,b], Jakub Kierdaszuk [a], Aneta Drabińska [a], Tanvi Karpate [a], Maciej Głowacki [d], Mateusz Ficek [d], Wojciech Gawlik [c], Ryszard Buczyński [a,b], Adam Wojciechowski [c], Robert Bogdanowicz [d], Mariusz Klimczak [a,*]

[a] Faculty of Physics, University of Warsaw, Pasteura 5, Warsaw, 02-093, Poland
[b] Łukasiewicz Research Network - Institute of Microelectronics and Photonics, Al. Lotników 32/46, Warsaw, 02-668, Poland
[c] Institute of Physics, Jagiellonian University in Kraków, Łojasiewicza 11, Kraków, 30-348, Poland
[d] Faculty of Electronics, Telecommunications and Informatics, Gdańsk University of Technology, Narutowicza 11/12, Gdańsk, 80-233, Poland

ARTICLE INFO

Keywords:
Diamond particles
Nitrogen-vacancy centers
Magnetic sensing
Optical fibers

ABSTRACT

Integration of optically active diamond particles with glass fibers is a powerful method of scaling diamond's magnetic sensing functionality. We propose a novel approach for the integration of diamond particles containing nitrogen-vacancy centers directly into the fiber core. The core is fabricated by stacking the preform from 790 soft glass canes, drawn from a single rod dip-coated with submicron diamond particles suspended in isopropyl alcohol. This enables manual control over the distribution of nanoscale features, here – the diamond particles across the optical fiber core. We verify this by mapping the diamond distribution in the core using confocal microscopy. The particles are separated longitudinally by 12–29 μm, while in the transverse plane a separation of approximately 1.5–2.2 μm is observed, corresponding to the individual cane diameter in the final fiber, and without significant agglomeration. The fiber's magnetic sensitivity is confirmed in optically detected magnetic resonance recorded with a coiled, 60-cm-long fiber sample with readout contrast of 1.3% limited by microwave antenna coverage. Moreover, magnetic-field dependence of the NV^- fluorescence intensity is demonstrated in the absence of microwaves, allowing magnetometric applications with a large (from 0 to 35 mT) B-field dynamic range.

1. Introduction

Sensing functionalities of diamond encompass electrical, magnetic, and dielectric interaction with matter and can be shaped by chemical modification and the size of the diamond crystals [1]. Appropriate doping using plasma-enhanced chemical vapor deposition (CVD) has opened means for modification of diamond's refractive index and conductivity [2]. The latter facilitates the use of diamond in electrochemical sensorics as an ultrawide bandgap semiconductor with electron mobility exceeding 2000 cm^2/Vs [3,4]. Incorporation of nitrogen-vacancy color centers (NV^-) in such sensors unfolds novel magnetic properties, and can be realized by either CVD, or other methods, such as graphite-to-diamond phase transition under high pressure and high temperature (the HPHT method) or the detonation of diamond crystals mixed with CaHbNcOd-type compounds [5–7].

Practical sensor devices based on NV^--doped diamond require integration with structures that would leverage the scaling up of different sensing modalities. For example, the pick and drop method can be used to transfer crystalline diamond particles from the growth substrates onto various flexible platforms overcoming the intrinsic brittleness of diamond in strain sensors sensitive for strains below 0.1 [8]. The possibility of an optical readout of diamond's magnetic response in the optically detected magnetic resonance (ODMR) technique motivates the integration of diamond particles with optical fibers. Implementations involving fiber tip deposition or various evanescent field realizations like fiber tapers are intensively investigated with nano- or microdiamonds containing NV^- or other color centers [9–11]. Fiber tip functionalization with color center nanodiamonds has been demonstrated in micrometre-scale spatial resolution, non-contact thermal mapping application with 20 $mK/\sqrt{Hz}$ thermal resolution [12]. Prior

* Corresponding author.
E-mail address: mariusz.klimczak@fuw.edu.pl (M. Klimczak).

https://doi.org/10.1016/j.carbon.2022.04.024
Received 19 August 2021; Received in revised form 4 April 2022; Accepted 8 April 2022
Available online 11 April 2022

designs of photonic crystal fiber tip functionalization with NV^- nanodiamonds were demonstrated in the context of optical adjustment-free single photon sources [13]. These results revealed impressive NV^- fluorescence collection efficiency with fibers, which was comparable to far-field imaging through an objective with a numerical aperture larger than 0.8. NV^- fluorescence collection efficiency in the range of 35–37% was reported for tapered single-mode fibers, in which the tapered section was in direct contact with a diamond micro-waveguide for designing possible single photon emitters and efficient quantum optics interfaces [10,14]. These implementations relate to ultra-sensitive, highly localized interaction of NV^- emitters with the surrounding. Fluorescence collection of NV^- centers in diamond over extremely distributed sites in the tens-of-meters scale was also demonstrated using a fiberized setup [15]; however, in this implementation the NV^- fluorescence was collected by photodiode chips distributed along 90 m length of a fiber capillary, in which a droplet with a single microdiamond particle was pushed along by applied air pressure.

Recently, the volume incorporation of diamond micro- and nanoparticles into a glass and subsequent drawing of optical fibers has been proposed as a radically alternative method of scaling of NV^- emission yield [16,17]. Although theoretically straightforward, it is hindered with oxidation and graphitization of diamond particles during the high temperature processing steps, including glass melting and fiber drawing at a tower. The choice of glass hosts is thus limited to low melting point soft glasses and indeed the first demonstrated diamond particle volume-doped glass fibers were drawn using tellurite glasses with melting (diamond incorporation) and drawing temperatures of 610 °C and 400 °C, respectively [17,18]. It has to be noted, that tellurite glass fibers are tedious in handling, especially to non-experts in specialty fiber development, due to the poor mechanical properties of the glass itself. Alternatively, silicate soft glasses can be used, like the F2 lead-silicate glass (Schott), which albeit requiring a higher drawing temperature around 700 °C, possesses superior mechanical robustness compared to tellurite glasses [19].

The thermal stability of the nanodiamond plays a critical role during integration with glass. Qiao et al. manifested that nanodiamonds undergo graphitization into onion-like forms during annealing at 1400 °C for 1 h in atmosphere [20]. Furthermore, it has been shown that the decomposition of oxygen-containing groups occurs at 300–900 °C, while CH_x groups decompose at 700–1150 °C [21]. The micrometre-sized diamond exhibits elevated resistance to graphitization at temperatures of 700–1400 °C under pressures in the range of 2–8 GPa [22]. Such nanodiamonds decompose less effectively to graphite than the onion-like structures, forming preferably the microcrystalline graphite.

Butenko et al. [23] reported that graphitization is driven by two main mechanisms dominating in the specific temperatures. The Debye temperature of nanodiamond (1577 °C) results from the boundary of these two thermal ranges: (I) – penetration from the surface in-depth of bulk region of diamond particle and (II) – abstraction of the surficial groups stabilizing the crystal edges. Thus, the thermal conductivity of nanodiamond is an important indicator of the diamond–graphite equilibrium [24]. Thermal decomposition or oxidation of diamond particles are not the sole concerns when the volume incorporation in optical fibers is considered. Importantly, Tsukahara et al. [25] revealed that aerobic oxidation of nanodiamond at 550 °C is responsible for improving the transverse spin-coherence time (T2) of NV centers, which enhances their sensitivity in quantum sensing. In the specific fiber context, melting of bulk soft glass for fiber preform components from raw materials, with adding the diamond particles during the melting, results in random distribution of the nanodiamonds in the obtained samples [16]. Authors in Ref. [26] have revealed with advanced modelling, that magnetic sensitivity of nanodiamond-doped fiber probes could be increased in comparison to isotropic diamond-doped materials by optimizing the fiber's various parameters, including core-cladding index contrast and the position of diamond emitters in the fiber core or the core-cladding interface.

In this work, we report on a novel volume incorporation approach for the integration of nitrogen-vacancy centers-containing submicron diamond particles with optical fibers. A step-index fiber is developed by stacking the core preform from 790 canes made of lead-silicate glass, which after drawing at a fiber drawing tower, constitute a solid fiber core. The canes have been drawn from a single glass rod dip-coated with crystalline diamond particles containing NV^- centers suspended in isopropyl alcohol, similarly to the method proposed earlier [14]. The diamond-coated cane stack was inserted in a tube made of thermally matched silicate glass and drawn at a fiber drawing tower into a final multimode, step-index fiber with 50 μm core diameter and 125 μm outer diameter. Mapping of physical distribution of the diamond particles embedded in the fiber core has been performed using confocal microscopy imaging, revealing even distribution of single crystalline diamond particles across the fiber core with only minor, isolated agglomerates. The developed fiber was tested in two experiments involving its magnetic sensitivity stemming from the presence of the NV^- diamond particles in its core. In one scenario the fiber was spun on a microwave antenna and optically detected magnetic resonance was measured with readout contrast of up to 1.3%, which was scalable with and limited by the coverage of the fiber by the antenna. In the second test experiment, we measured NV^- fluorescence intensity change in a 35 mT dynamic range of magnetic flux density from an electromagnet.

2. Experimental methods

2.1. Submicron diamond particles-incorporated optical fiber fabrication

The optical fiber development procedure begun with the preparation of preform components, which included the cladding tube and a solid glass rod for fabrication of the diamond-coated glass canes constituting the fiber core stack. F2 lead-silicate glass (Schott) was selected as the base fiber glass and specifically, it was used for the diamond particle functionalization and core stacking. Nominally, the lead-silicate F2 glass contains between 40 and 50 wt % each of silica and lead oxide, which are complemented by up to 10% each of potassium oxide and sodium oxide and below 1% of arsenic trioxide. Its refractive index is $n_1 = 1.6199$ at the wavelength of 589.3 nm. A modified composition within the above limits was melted in-house in the form of a tube, with the (linear) refractive index $n_2 = 1.6133$ at the wavelength of 589.3 nm. This glass was used for the cladding tube of the fiber preform. An index-guiding fiber was thus possible to obtain from these materials.

The actual fabrication procedure was split into four steps, which are schematically shown in Fig. 1a. The first involved integration of diamond particles with the glass rod. We adapted the dip-coating approach reported earlier by D. Bai et al. [19]. The diamond particles used for coating were suspended in isopropanol, with the diamond concentration of 0.05%. We used submicron diamonds with an average particle diameter of 750 nm (MDNV1um, Adámas Nanotechnologies), which is a compromise between fluorescence yield and scattering loss introduced by the particles in the core of the optical fiber. To verify size distribution of the particles used in this study, the diamond suspension was placed in a disposable, polystyrene cuvette (outer dimensions of 12 × 12 × 45 mm), and examined using the Zetasizer Nano ZS particle analyzer (Malvern Panalytical, UK) equipped with a 632.8 nm laser. Measurements were performed at 25 °C using backscatter configuration (light collected at 173° angle). The viscosity and the refractive index of the dispersant (isopropanol) were set at 2.038 cP and 1.377, respectively [27,28].

Before dip-coating, a cylindrical cuvette with the diamond particles suspension was stirred in an ultrasonic cleaner for 20 min and then was moved onto a magnetic stirrer for 3 min. The cuvette was then placed again in an ultrasonic cleaner for 5 min, and again for 3 min on the magnetic stirrer. Then the cuvette was placed in the ultrasonic cleaner for the final 5 min. After this, the F2 glass rod (diameter of 30 mm) was slowly immersed in the diamond suspension in the cuvette. After lifting

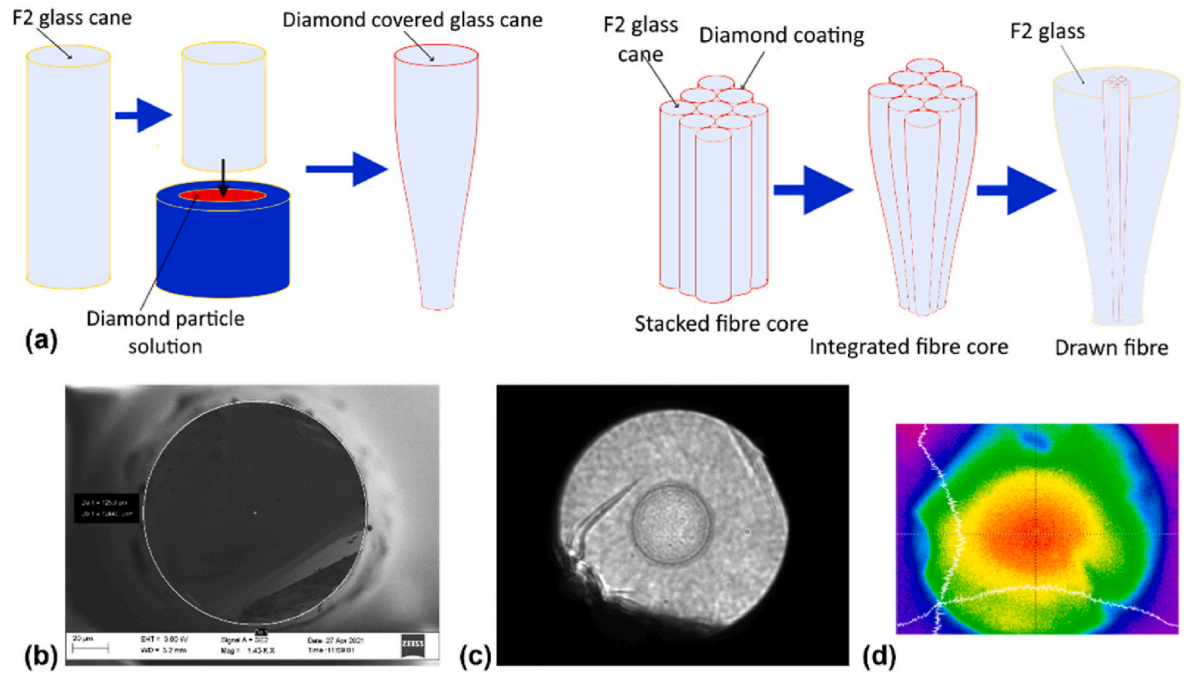

Fig. 1. Submicron diamond particles-doped nanostructured core fiber: (a) fiber development procedure, (b) scanning electron microscope image of the fiber, (c) optical microscope image of the fiber, (d) mode field image of the fiber output over a red high-pass filter.

from the cuvette, the excess liquid was allowed to drain back into the cylinder and residual isopropanol to evaporate from the surface of the glass rod. This coating procedure was repeated 10 times.

In the second step, the dip-coated F2 glass rod was drawn into canes. To ensure that no contaminants were present in the fiber, the coated glass rod was placed in the drawing tower furnace and then heated up to 400 °C in a dry oxygen atmosphere. This temperature is high enough to burn most small contaminates on the glass surface, while leaving the diamond particles intact. This was verified before dip-coating by thermogravimetric analysis (TGA) of the diamond powder, which indicated mass change related to oxidation at temperatures exceeding 550 °C. F2 glass fiber drawing requires a higher temperature of around 700–750 °C, which is unacceptable for diamond in an oxygen atmosphere. However, TGA reveals that diamond mass change of only 0.5% occurs at this temperature range when the oxygen atmosphere is replaced with nitrogen. A nitrogen atmosphere was thus introduced to the furnace and the temperature was increased to 740 °C. After the start of the drawing process of the diamond-coated rod, the temperature was reduced to 710 °C and the rod was drawn at that temperature. The rod was drawn from 30 mm diameter down to 0.5 mm ± 0.02 mm canes. In the third step, the drawn canes were cut to 12 cm length and stacked inside the in-house prepared glass tube with an external diameter of $d_e = 40$ mm and an internal diameter of $d_i = 16$ mm. 790 glass canes were fitted inside, forming the structured glass preform. The preform was then drawn at the drawing tower from the initial diameter down to a 4 mm diameter structured rod. During this process, the nitrogen atmosphere was again introduced into the furnace. Additionally, after the drawing process had started, low vacuum was introduced selectively to the core stack to ensure integration of the individual submicron diamond-coated canes. This was crucial during this part of the drawing, because the rough diamond coating of the individual rods traps atmospheric gasses between canes and leads to uneven glass integration. In the final step the structured rod with a fully fused, diamond particles-doped core was drawn into the final fiber. The external diameter of the fabricated fiber is $d_f = 125$ μm (excluding the protective acrylic coating), while the diameter of the core is $d_c = 50$ μm. During the drawing, the diameter of the fully fused canes in the core stack was decreased to $d_r = 1.5$ μm. The scanning electron microscope image of the fiber is shown in Fig. 1b. Due to low refractive index contrast, the core area is indistinctive from the cladding, although it can be well seen under a standard optical microscope, which is shown in Fig. 1c. The mode field of the red fluorescence of NV^- color centers, filtered with a red high-pass filter to cut out the 532 nm laser pump, is shown in Fig. 1d.

Normally, the fiber drawing is carried out at a temperature at which viscosity η of the glasses used in a preform is between $\log\eta = 7$ and $\log\eta = 8$. Here, the set drawing temperature (720 °C) is higher than sphere creation temperature T_{sph} for either of the glasses (690 °C for the core glass F2, 710 °C for the cladding glass, a detailed table with measured glass parameters is contained in the Supplementary Information). The reason for that is the placement of the thermocouple in the furnace, near the heating elements. At the center of the furnace, where the glass is located, this temperature is lower by roughly 70 °C, thus the fiber is actually drawn at a temperature of about 650 °C. The glass used in the core is closer to its sphere creation temperature T_{sph} than the cladding glass, which means that its viscosity is lower. Additionally, the difference in coefficients of thermal expansions of both glasses should be smaller than 10%, as is in the case of our process, in order to avoid cracking or separation of the glass during cooling. We note that the fiber reported by authors in Ref. [19] was developed from the same glass type in the core and cladding, which contributes to explaining the difference in the final fiber fusion between our case and the fiber described in Ref. [19].

2.2. Diamond particles-incorporated optical fiber attenuation

The attenuation of the developed fiber was measured using the cut-back method in three separate measurements carried out at wavelengths of 532 nm, 780 nm, and 1560 nm. Measured attenuation was 81 dB/m at 532 nm, 49 dB/m at 780 nm, and 32 dB/m at 1560 nm. These loss figures are comparable only to the higher-loss end of the tellurite glass fibers reported in Ref. [17]. We note that the best diamond-doped tellurite fibers reported in Ref. [17] with decreased diamond concentration (compared to the more densely doped samples reported therein) exhibited background loss of around 10 dB/m. Compared to the interface-doped fiber (diamond particles located at the core-cladding interface) reported by D. Bai et al. in Ref. [19], the loss measured in

our fiber is roughly an order of magnitude higher, despite the same glass type used and a comparable diamond particle size, i.e. 1 μm diameter in Ref. [19] and around 750 nm diameter in this work. Results reported for fibers either with 45 nm diamond particles or with 1 μm particles in the optical fiber core confirmed that the larger diamond particle size enhanced NV^- fluorescence yield due to larger NV^- color center number [17,19]. However, in the case of our fiber, the large particle size also contributes significantly to scattering loss of the guided modes. The fiber core, where the light is guided, in this work can be considered as a particle suspension, where the particles – the submicron diamonds – are suspended in a solid – the glass. Absorption of the NV^- centers cannot be assigned to the entirety of the recorded loss level, especially at the red wavelengths. Light scattering should be considered with respect to the relation of the light wavelength to the diamond particles mean size and the particle-to-particle separation. The diamond-to-diamond separation in the propagation direction of the fiber core (discussed in detail in the following section) indeed exceeds the wavelength by an order of magnitude, but in the transverse plane of the core it is only between 1.5 and 2.2 μm, which is two to three wavelengths. The particle size, i.e. the mean size determined with the dynamic light scattering method, was around 750 nm, which is comparable to the wavelength of NV^- emission (zero-phonon line at 637 nm). Therefore, the main loss mechanism of the propagating mode would be the diffraction at the glass-diamond interface, caused by the large difference of the F2 glass and diamond refractive indices. Since the major fraction of diamond particles has their size comparable to the wavelength, the main mechanism should be the Mie scattering, which is supported with strong back-reflected 532 nm pump signal, which could not be explained by the Fresnel reflection alone. A small fraction of the diamond particles used in the work had size smaller than the mean 750 nm (as discussed in the following section), thus the contribution of Rayleigh scattering cannot be entirely excluded. The presence of both these scattering phenomena is supported by the increasing attenuation measured in the fiber for decreasing wavelengths. We note that in recent work involving wavelength-sized gold nanoparticles or sub-wavelength silica nanoparticles in liquid suspensions, Brillouin scattering (and backscattering) has been reported, although we have not observed evidence of that under our experimental conditions [29,30]. The future realizations of fibers exploiting the concept described in this work should explore a tradeoff between diamond particle size and expected NV^- fluorescence yield, as well as the fiber volume effectively interacting with the microwave field.

3. Results and discussion

3.1. Submicron diamond particles fluorescence and spatial distribution in the fiber

In the preceding part, we have demonstrated that one of the key challenges in the diamond particles-doped fiber drawing from dip-coated glass preforms involving successful integration of preform glass components in presence of a diamond layer, can be solved by selective application of vacuum to the optical fiber core area. The obtained, fully fused, diamond particles-doped fiber core has also been demonstrated to couple NV^- color center fluorescence into its guided modes. In this part of the study we discuss the properties of the submicron diamond particles used in the work, as well as the details of their distribution in the optical fiber core.

Fig. 2a depicts a high-magnification scanning electron micrograph of the diamond particles used in this study. Particles are characterized by irregular shapes with sharp corners, as expected from diamond crystals

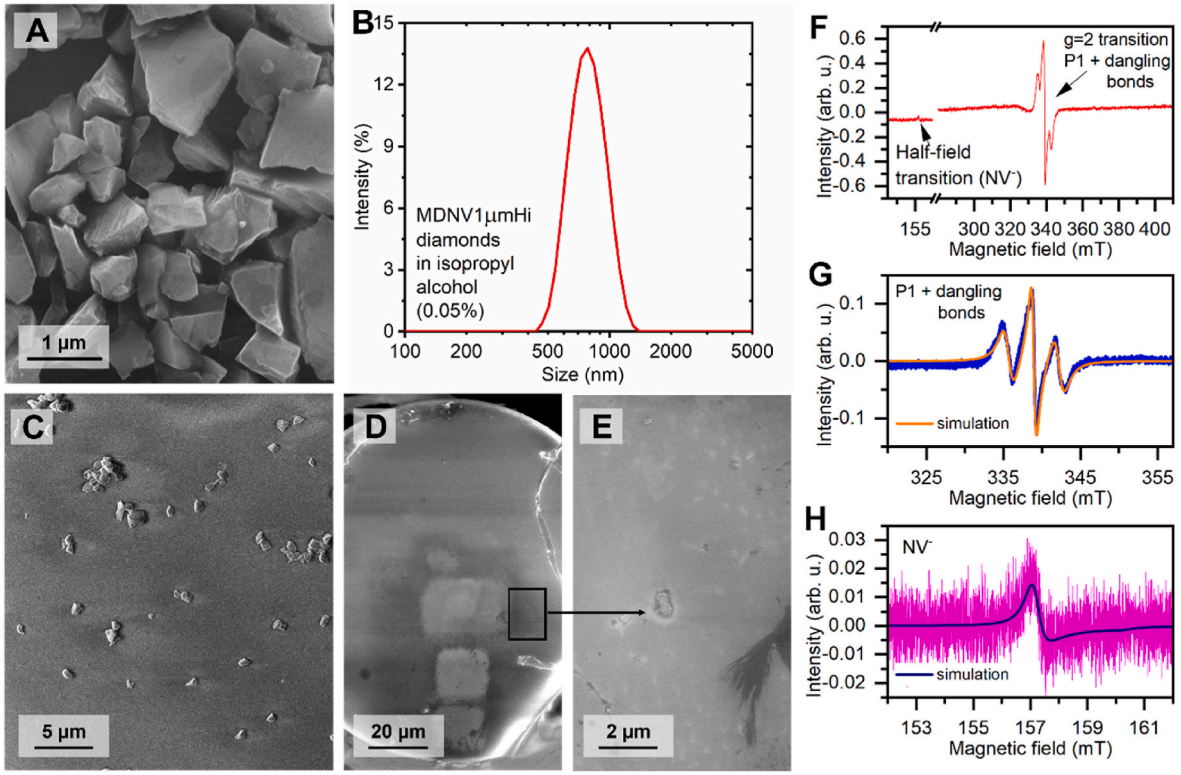

Fig. 2. Submicron diamond particles in nanostructured core fiber and EPR results of X band (recalculated to 9.5 GHz) of diamond powder measured at 5.4 K: (A) SEM image of diamond particles deposited on the surface of a polished F2 glass plate by dip-coating, (B) particle size distribution in the diamond suspension used in the dip-coating procedure, (C) SEM image of F2 glass plate surface dip-coated with diamond particles, (D), (E) cross-sectional images of the drawn fiber, (F) wide range EPR spectrum measured for 474 μW of microwave power, (G) g = 2 spectral region of EPR spectrum measured for 1.5 μW of microwave power with its simulation, (H) EPR spectrum of the half-field transition measured for 4.7 μW of microwave power with its simulation. The simulations were performed using EasySpin software [33].

produced using the high-pressure high-temperature method and then crushed to finer particles [31,32]. The surfaces of the particles are marked with large roughness and crystalline fractures. To examine the size distribution of the diamond particles shown in Fig. 2a, and to verify if agglomeration of the particles occurs at an early stage of the technological procedure, the starting suspension was investigated after its homogenization by dynamic light scattering. The resulting particle size distribution presented in Fig. 2b was averaged from three consecutive measurements. The distribution is monomodal as there is only one peak visible. A fraction of the particles with sizes ranging from around 440 nm to 1400 nm with the maximum signal at 780 nm is observed. The system has not registered any larger, sedimentation fractions. Next, to validate whether agglomeration occurred at the surface of the glass during and immediately after the rod dip-coating procedure, a series of reference square plates (20 × 20 × 1 mm) made of the F2 lead-silicate glass was covered with the diamond particles (Fig. 2c). The analogous procedure was utilized during dip-coating of the initial F2 glass rod. The morphology of the F2 plates displayed in Fig. 2c reveals distinctly that the majority of the glass area is covered with single, separated diamond particles. Individual diamond particles could create small-scale agglomerates, but they account for a minor proportion of the overall coverage and also tend to separate in the fiber drawing step. The typical distance with neighboring diamond particles on the dip-coated glass surface ranges between 2 μm and 5 μm. Fig. 2d presents the diamond-doped fiber cross-section revealing a homogenous glass structure with sectionally incorporated diamond particles (attn. zoomed image in Fig. 2e). The diamond particles are tightly included in the glass structure with a mean adjacent distance of approximately 2.5 μm. No larger agglomerates or gas bubble defects were observed during SEM imaging studies. The Supplementary Information contains a detailed calculation of theoretical mean distance between the adjacent diamond particles of the dip-coated glass rod surface. Considering the size of the initial F2 glass rod used for fiber core stacking and drawing, and assuming 20 μm as the mean distance between two adjacent diamond particles in the final fiber, as discussed in the next section (based on confocal imaging data), the mean distance between adjacent diamond particles at the surface of the initial F2 glass rod can be calculated as 2.6 μm, which agrees with experimental observations. Electron imaging data correspond to optical microscopic experiments and both support the statement against considerable agglomeration of the diamonds in the developed fiber.

After the study of the agglomeration of diamond particles on F2 glass, two measurements were carried out to assess the concentration of nitrogen and NV^- color centers in diamonds used for fiber development. First, the presence of paramagnetic centers in the diamond particles (1.5 mg) was verified by continuous-wave electron paramagnetic resonance (CW EPR) spectroscopy. Measurements were performed in a Bruker EPR ELEXSYS E580 spectrometer equipped with a TE_{102} cavity and a cryostat allowing measurements at the liquid helium temperature. Fig. 2f presents a wide-range EPR spectrum of submicron diamond particles measured at 5.4 K. It consists of an intense line in the g = 2 region and a weak line corresponding to the half-field transition. A precise measurement of the g = 2 region is presented in Fig. 2g. A simulation performed with EasySpin software extracted two contributions to this signal: one related to the P1 centers and the second – weaker – related to dangling bonds [33,34]. The P1 centers are substitutional nitrogen defects that can recombine with a vacancy and form the NV^- center [35]. Hyperfine coupling to the ^{14}N nuclear spin (I = 1) results in the formation of three intense lines near the g-factor of 2. The spin counting procedure in the EPR spectrometer software together with a ratio of double integrals of the P1 and dangling bonds signals obtained from a simulation allowed to estimate their concentration at 6.5 ppm for the P1 center and 0.8 ppm for dangling bonds. The allowed transitions of the NV^- center are characterized by satellite lines in the g = 2 region [34,36]. However, the random orientation of microcrystals in the diamond powder samples and the associated line broadening significantly decreases the intensity of lines to the point that it is often not possible to observe them experimentally [34]. Therefore, only a weak half-field line related to forbidden transition is present in the spectrum as shown if Fig. 2h. The concentration of the NV^- centers equal to 0.2 ppm was estimated by the spin counting procedure in the EPR spectrometer software for the half-field transition and by multiplying the result obtained by a factor estimated from the simulation of the measured NV^- spectrum in the EasySpin software [33,37]. Because of the low intensity of the half-field transition and the saturation observed at increased microwave power, the spectrum was measured at the lowest microwave power for which the signal was distinguishable. We note however, that it was unclear if the measured line is already partially saturated. Therefore, the uncertainty of the NV^- centers concentration estimation in the EPR spectrometer is large and the obtained value should be considered as the lower limit of concentration while the real concentration should be expected at a higher level. To confirm this, in the second measurement, the fluorescence signal of the MDNV1um diamond particle was compared to the one from a reference diamond plate sample (DNV-B1, Element6). NV^- fluorescence excited at a wavelength of 561 nm (limiting the influence of NV^0) was recorded using a commercial confocal microscope system (Olympus FV3000×HSD, 60 × oil objective with NA = 1.42). This allowed us to probe a confocal volume (roughly 0.3 × 0.3 × 1 μm) within a single diamond particle. The reference sample plate is specified for the concentrations: [N] = 0.8 ppm, [NV^-] = 0.3 ppm. From the approximately 10 × higher fluorescence intensity collected from MDNV diamonds, we estimate the NV^- concentration at 3 ppm, which matches the vendor data (MDNV1um, Adamas Nanotechnologies) provided for this material. This would also imply a conversion efficiency of nitrogen to NV centers of around 24%, assuming there is also positively charged nitrogen in the lattice in a similar amount ([N+] = 3 ppm), which is EPR silent and acts as a donor for the NV^- centers. Although this is a relatively high figure, and we consider the corresponding NV concentration as an upper limit, we note that similar and larger conversion efficiencies have been observed [37,38].

The next part of the work moves on to reporting results of spatial, i.e. the transverse and longitudinal mapping of the diamond particles distribution in the fiber core. Characterization of the distribution of diamond particles in the developed F2 glass fiber (and the fiber's sensing potential described in the following section) was carried out using the confocal microscopy technique. Three-dimensional scans were recorded with a commercial confocal microscope system (Zeiss LSM710). A 4 mm-long section of the fiber was placed on a microscope slide surrounded with immersion oil (n = 1.52). Fig. 3a schematically shows the diamond mapping arrangement with the principal planes of imaging. The propagation direction along the fiber was in the Y axis, while the transverse plane of the fiber was located at the XZ plane. A 3-D image viewed from the YZ plane – shown in Fig. 3c, i.e. along the propagation direction along the fiber, was acquired by stacking 137 individual images in the XY plane with a 0.5 μm step along the Z axis. The image height is around 68 μm, which just slightly exceeds the core diameter of 50 μm. The fiber was imaged using seven different sample sections, separated by around 10–15 cm in the original fiber. The length of each sample image under the confocal microscope was around 354 μm, which stemmed from the size of the field of view of the microscope system. The bright spots correspond to the submicron diamonds and their spatial distortion in the image is caused by astigmatism due to the difference of around Δn = 0.09 between the fiber refractive index and the surrounding immersion oil. The transverse, XZ plane of the fiber is shown in Fig. 3b. The core is outlined with a yellow circle. The image shows the transverse distribution of the diamonds corresponding to the longitudinal distribution shown in Fig. 3c over 354 μm length of the fiber. Both the longitudinal and transverse plane images enable distinguishing single diamond particles in the volume of the fiber core without significant agglomerations despite one, which is manifested as a brighter spot, located around 80 μm from the fiber sample facet and slightly offset from the fiber core center.

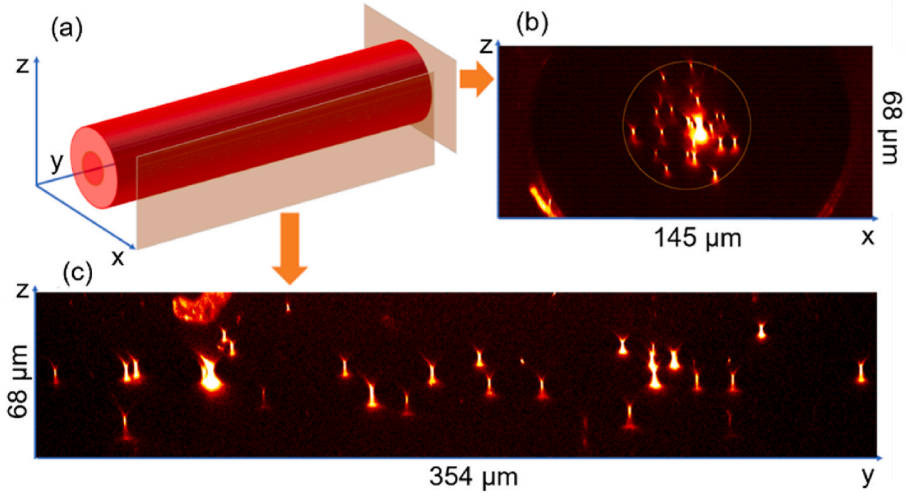

Fig. 3. Confocal microscope scan of a section of the developed fiber: (a) schematics of the fiber sample with the imaging planes marked, (b) diamond fluorescence recorded for the XZ plane, and (c) the YZ plane.

To evaluate the diamond particle distribution in the fiber core in a quantitative manner, we measured the distances between the immediately (directly) adjacent diamond particle pairs along the optical fiber and also across its core. Details on the methodology of this part of experiment are described in the Supplementary Information. In the longitudinal plane of the fiber, the major observed share of diamond particle pairs are separated by between 12 µm and 29 µm. Diamond-to-diamond separations outside of this range are also observed, but with smaller contribution to the histogram (which is shown in Fig. S1a in the Supplementary Information). In the transverse plane, the diamond separation of roughly 1.5–2.2 µm dominates (shown in the histogram in Fig. S1b in the Supplementary Information), which almost ideally corresponds to the 1.5 µm diameter of the estimated individual cane diameter in the final fiber core.

Seal [39] revealed that 1 µm-sized diamond particles lose their diffraction pattern at temperatures of about 2000 °C. Lower temperature treatment results only in partial and local graphitization mostly depending on the irregular arrangement of carbon atoms inducing formation of diamond-like and graphite-like regions. It was found that the diamond graphitization pathways could be modified and catalysed by metal impurities common in the HPHT crystals. Tulić et al. [40] showed that nickel caused enhanced 2-dimensional etching of (110) and (100) facets of diamond, where (111) lattice exhibits the highest stability. Obviously, larger diamond crystal sizes showed larger activation energy for graphite phase transition [22], resulting in heterogenous character decomposition, thus only particular regions of a diamond particle would be graphitized, while other sections remained unharmed.

Butenko *el al.* [23] revealed graphitization rates utilizing a "reducing sphere" model and Arrhenius expression estimation. The activation energy of $E = 45 \pm 4$ kcal/mol is required for graphitization resulting in maximal rates of $A = 74 \pm 5$ nm/s at range of 1000–1500 °C, which are relatively low considering utilized micrometre-size diamond particles. Next, the use of cane stacking creates a barrier limiting the direct diamond exposure to the thermal sources and spreads the heat over a large area of glass surface.

Multiple cane stacking has also an important advantage in the context of this characteristics because replacing diamond-coated canes with pure glass canes in the stack enables manipulation of the transverse distribution and provides means of e.g. controlling the diamond particle concentration at specific areas of the fiber core. Table 1 contains a summary of the recently demonstrated magneto-optic fiber probes with diamonds incorporated into the volume of the fiber core, either by direct melt doping, or by the dip-coating technique reported earlier by D. Bai et al. in Ref. [19] and which underpins the development procedure of the fiber demonstrated in our work.

Table 1
Summary of fabrication, structural and magnetic sensing characteristics of realized magneto-optic fiber probes with core areas doped with diamond particles.

Characteristic	Tellurite glass step index fibers [17,18]	F2 glass fibers with a diamond particles ring [19]	F2 glass nanostructured submicron diamond doped fibers [this work]
Diamond particle size	45 nm	1 µm	750 nm
Temperature during diamond incorporation into glass	610 °C	660–690 °C	710 °C
Fiber drawing temperature	400 °C	660–690 °C	710 °C
Core/cladding refractive indices	Single glass, either 1.98 or 2.00 (at λ = 1064 nm)	Single glass (F2), 1.6199 (λ = 589.3 nm)	1.6199 (core) and 1.6133 (cladding), λ = 589.3 nm
Diamond incorporation technique	ND powder added to glass melt	Dip-coating of fiber core preform, followed by drawing	Dip-coating of core preform canes, followed by drawing multiple canes together
Diamond distribution – longitudinal	Random, further diluted during drawing	Random, further diluted during drawing	Random, dilution during drawing present but outweighed by cane stacking
Diamond distribution – transverse	Random	Determined by circular shape of the core preform, randomized along core circumference	Determined by cane diameter in final fiber core, controllable by cane stacking
Demonstrated magnetic field sensing performance	ODMR read-out contrast of 3.5% (point excitation of fiber)	ODMR read-out contrast of 2.5% (point excitation of fiber)	ODMR read-out contrast of 1.3% MW-free B-field measurement with 35 mT dynamic range

3.2. *Proof-of-principle fiber magnetometry*

In the final part of the work, the developed fiber was evaluated for its

applicability in magnetic sensing. Two types of experiments were carried out, both involving a 60 cm-long fiber sample. The first one was measurement of the optically detected magnetic resonance (ODMR), followed by measurement of the dependence of diamond fluorescence intensity on the magnetic field without presence of microwaves. We begin with the ODMR experiment and the setup used in this part is shown in Fig. 4. Optical readout of the fiber's magnetic response was realized under excitation from a 532 nm continuous-wave laser (Sprout-H). The green light was coupled into the fiber from both ends: on one end a standard collimating lens was used, and on the other light was coupled through a dichroic mirror (Thorlabs DMLP567) and a microscope objective (Olympus UPLFLN 40 ×, NA = 0.75). The NV^- diamond fluorescence was separated from the green light at the dichroic mirror and residual 532 nm signal was filtered out using a 600 nm high-pass filter (FEL0600, Thorlabs). The NV^- fluorescence was detected with a Si avalanche photodetector (APD130A, Thorlabs). This setup allowed effective detection of fluorescence over a wavelength range of 600–850 nm, as well as comparing the excitation efficiency from either end of the fiber sample. In order to observe the optically detected magnetic resonance (ODMR), a microwave (MW) oscillating field at the frequency around 2.87 GHz was generated using a signal generator (SRS, SG386) and a high-power amplifier (Mini-Circuits ZHL-16W-43+) connected to a loop-gap type antenna structure on a printed circuit board [41]. One fiber end was passed through the opening in the center of the antenna loop which allowed the interaction of this fiber section with the MW field. Fluorescence and ODMR signals were then observed on an oscilloscope.

Optical fluorescence spectra of the investigated NV^- fiber samples were recorded using a compact grating spectrometer (AvaSpec-3648-USB2, Avantes). The spectra, shown in Fig. 5, were collected in two configurations. In the first one, excitation and detection took place from the same end of the fiber – this was realized with the shutter 1 open, Fig. 4. In the second measurement, the excitation and detection occurred from the opposite ends of the fiber – the shutter 2 was opened, Fig. 4. The ZPL line characteristic of the NV^- is noticeably dominated by phononic sidebands at room temperature [42], and phonon interactions are only suppressed at cryogenic temperatures. Additionally, we work with submicron diamond particles, where the optical NV^- spectra deviate from a typical bulk-diamond NV^- spectrum because the size becomes comparable with light wavelength. This is one of the factors that affect the visibility of the ZPL [43]. The recorded signal was normalized to the intensity at the ZPL wavelength. Normalization based on the intensity of the diamond Raman band is another common mean of presenting the NV^- fluorescence spectra. However, this is feasible only for low-NV-density samples, where this line is clearly visible. In our case of highly-fluorescent particles, the presence of NV^0 fluorescence is overwhelming the diamond Raman line and precludes its observation. This is a common situation for the fluorescent diamond particle spectra

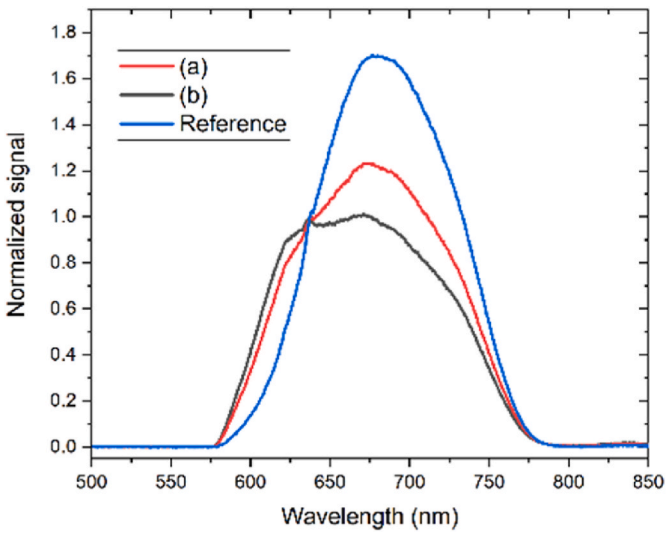

Fig. 5. Optical fluorescence spectra recorded with: (a, red) excitation and detection from the same end of the fiber, (b, black) excitation and detection from opposite ends of the fiber, (blue) unprocessed diamond particles.

[43]. The difference in the spectra shown in Fig. 5 is assigned to the wavelength-dependent fluorescence coupling into the guided mode and the scattering losses occurring during light propagation in the fiber when excitation and detection of NV^- color centers fluorescence occur at opposite ends of the fiber.

Among several sensing modalities enabled by NV^- color centers in diamond, the most common are measurements of magnetic field and temperature with the use of continuous-wave microwave field to drive the ODMR. Here, we realized a simple case of ODMR-based sensing of moderate magnetic field. ODMR readout was carried out in two configurations with the fluorescence excitation and detection taking place either for the same fiber end, or from the opposite fiber ends, while the microwave antenna was fixed near the detection side. Three magnetic flux densities were consecutively set in the measurements: 0 G, 15 G, and 21 G. The observed spectra are shown in Fig. 6. For the 0 G setting, the recorded ODMR spectrum did not differ significantly from the single-crystalline diamond, while in non-zero fields significant differences were recorded. The latter spectra are strongly inhomogeneously broadened by the random orientation of crystals with respect to the direction of the magnetic field [37]. The outermost edges of the spectra correspond to the diamonds with the maximum projections of the magnetic field, i.e., those oriented along the field direction. An approximately linear increase of the broadened spectrum width with the field strength can also be observed. The observed ODMR contrast value is limited to around 1% at zero magnetic field where no-inhomogeneous

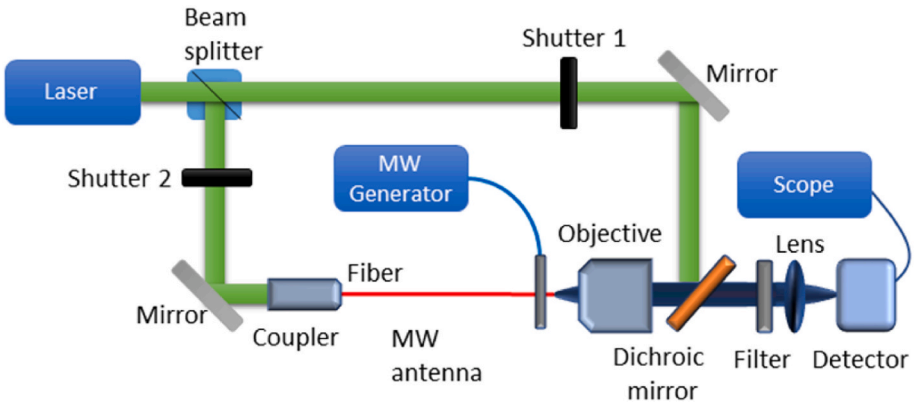

Fig. 4. Experimental setup for magnetic sensing experiments with the developed fiber.

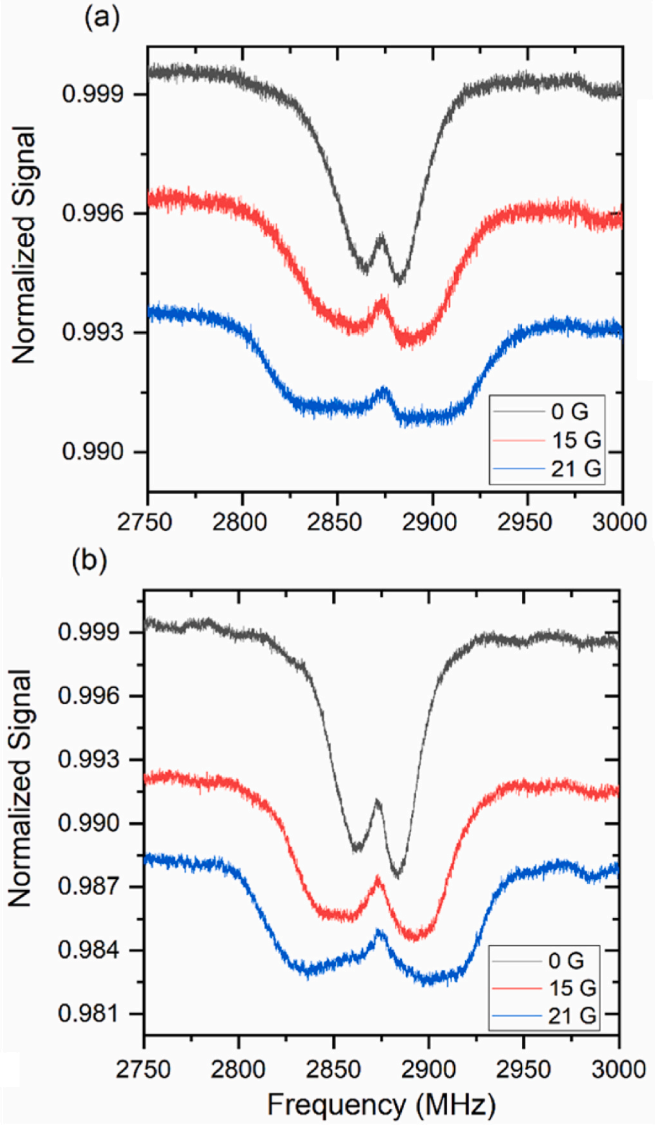

Fig. 6. ODMR spectrum collected in two configurations: (a) excitation from the same end of the fiber as detection and microwave antenna; (b) excitation by the guided light mode coupled from the opposite end of the fiber.

broadening is present and a single-frequency MW field drives all NVs regardless of their spatial orientation. This is due to the geometry of our microwave antenna, which effectively drives the NV^- spins over only several millimeters of the nearby fiber length, while the remaining fiber section contributes to the fluorescence background. When the fiber is interrogated locally from its side, the contrast value increases to above 5%, as is shown in the Supplementary Information. Additionally, we observe a factor of two contrast difference in the spectra recorded with the excitation light launched from both fiber ends. We attribute this difference to the placement of the microwave antenna at the detection-side end of the fiber, approximately 5 mm from the fiber end face, and different shapes of the green light mode when using opposite microscope objectives. In the epi-fluorescence excitation case, due to the fiber being spatially multimode and a relatively high NA objective being used, a different volume containing the submicron diamond particles is effectively excited than in the dia-fluorescence case. We emphasize, however, that the readout contrast could be improved by changing the antenna design for one acting on a longer section of the fiber or, alternatively, using a near-field of a microwave-current-carrying structure along the fiber.

We have also performed a proof-of-concept type of experiment demonstrating possibility of NV^- magnetometry with the developed fiber in a MW-free arrangement. In Fig. 7 we show the photoluminescence measured as a function of the magnetic field. To ensure the entire optical fiber interacts with a constant-strength magnetic field, the fiber was coiled into an approximately 3 cm diameter loop, as shown in the inset of Fig. 7, and placed axially under the neodymium magnet. The field strength was varied by changing the fiber-to-magnet distance and measured using a gaussmeter. The initial gradual decrease in photoluminescence is associated with a reduction of fluorescence emission of the NV^- centers misaligned with the magnetic field vector and occurs due to the spin-mixing by the transverse field components [44]. The observed decrease of fluorescence can be used for magnetometry with a 35 mT dynamic range and requires only a pre-calibration of the fluorescence levels. The randomized orientation of diamond particles inside the fiber makes it insensitive to the vector-orientation of the field, acting effectively as a scalar sensor. These results are in-line with the similar fluorescence changes reported for bulk diamond and with single NVs [44–46]; however, they do not match the dependency presented in Ref. [18], where also a volumetrically doped fiber was used but the fluorescence level with microwaves tuned off-resonance dropped more abruptly, within the 0–1 mT field range.

4. Conclusions

The main highlight of the work is achieving a uniform distribution of single, submicron diamond particles, which can be shaped across a step-index optical fiber core by stacking a core preform from glass canes. Their distribution in the transverse and longitudinal planes of the fiber were mapped in the volume of the core using confocal microscopy in seven fiber samples, taken from fiber sections 10-15 cm apart. Two main fractions in the diamond separation were identified, in the longitudinal plane, the majority of adjacent submicron diamond pairs was located between 12 μm and 29 μm apart, and in the transverse plane the separation was typically 1.5–2.2 μm, which corresponds with the estimated final (drawn fiber) 1.5 μm diameter of canes constituting the pre-final drawing core stack. We note that the total length of the fiber imaged for the longitudinal separation between adjacent diamonds was around 1 m. Thus, the provided statistics cannot support assuming the longitudinal particle separation to remain uniform along the total length of the drawn fiber, which was in the order of tens of meters. In contrast to

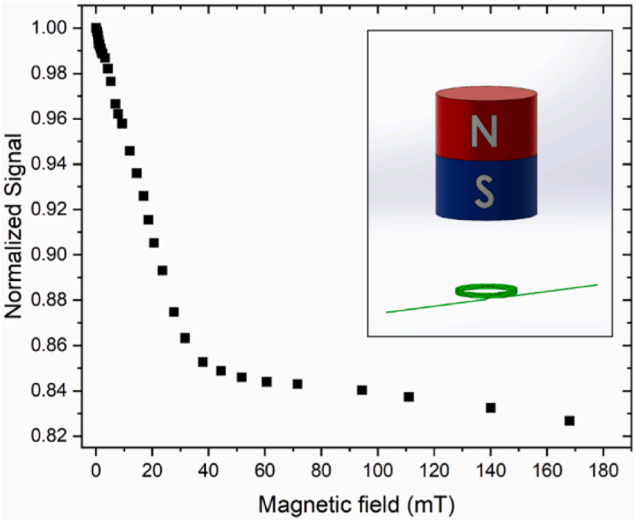

Fig. 7. Nitrogen-vacancy photoluminescence as a function of the applied magnetic field normalized to the photoluminescence at 0 mT. The inset shows the arrangement of the fiber coiled and placed axially under the permanent magnet.

previously reported implementations involving drawing of soft glass fibers directly from a diamond-suspension dip-coated glass preforms, stacking of multiple diamond-coated (and thinned at drawing temperature at a drawing tower) canes, combined with carefully adjusted drawing conditions, the fiber demonstrated in this work had fully fused core without airholes neither at the core-cladding nor at the intra-core interfaces. In addition to that, no evidence of significant agglomeration has been observed, despite the uniform distribution of the diamonds in the transverse plane of the core. The demonstrated stacking fabrication approach does not hinder the magnetic sensing functionality of the developed proof-of-concept fiber. We have verified this by recording ODMR spectra, in which the readout contrast (around 1.3%) was limited by the design of the microwave antenna used. However, it can be easily enhanced, e.g. using a microwave resonator which can effectively excite a centimeter-sized loop of optical fiber [47]. Additionally, we have demonstrated a microwave-free detection mode, in which fluorescence level can be mapped to the magnetic field value in a broad dynamic range of 0–35 mT.

In the context of NV^--fiber magnetometry, core nanostructurization carries two advantages. Firstly, it enables large degree of freedom in the positioning of the diamond particles relative to the transverse plane of the core for optimal coupling of the NV^- fluorescence to the fiber guided modes, which in our study is supported by the dominant fraction of diamond pairs separated by 1.5–2.0 μm, a distance roughly equivalent to the final size of an individual glass cane of the core preform stack. A recent theoretical study of this issue indicated significant coupling improvement by localization of the NV^- close to the cladding-core boundary [26]. Although the dip-coating distribution of diamonds on the glass surface of the initial preform component is generally random, we have observed that over areas largely exceeding the range of distances between adjacent particle pairs, the glass surface was covered uniformly with single crystals. Agglomerated diamonds could also be noted on the surface of dip-coated glass, but these were isolated instances. Control of the separation between the diamond particles in the final fiber is very limited by means of increasing their concentration in the dipping suspension.

The observed optical effects are determined and strongly depend on the interaction at the glass-diamond interface, which are stimulated by the surficial groups at the diamond as well as the surface termination of the amorphous glass. The micro- or even nanoscale interfaces might be furthermore investigated by high-cost, multi-scale molecular modelling or HR-TEM imaging since the oxidation and graphitization rates are tailored here considerably by limited oxygen atmosphere exposure thanks to the glass matrix encapsulation and short-term thermal treatment during fiber drawing.

Instead, using our approach, diamond assembling could be shaped by for example implementing core stack designs involving diamond-functionalized canes arbitrarily interleaved with pure glass canes. This methodology thus enables additional level of control over the transverse layout of the diamond particles. Following dedicated modelling and experimental work, it has the potential of extending the existing models with practical ways of optimizing NV^- fluorescence coupling to the guided modes in optical fiber-based ODMR and magnetometry probes.

CRediT authorship contribution statement

Adam Filipkowski: Methodology, Conceptualization, Formal analysis, Visualization. **Mariusz Mrózek:** Investigation, Formal analysis, Writing – review & editing, Visualization. **Grzegorz Stępniewski:** Investigation, Formal analysis. **Jakub Kierdaszuk:** Investigation, Formal analysis. **Aneta Drabińska:** Investigation, Formal analysis. **Tanvi Karpate:** Investigation. **Maciej Głowacki:** Formal analysis, Resources. **Mateusz Ficek:** Investigation, Formal analysis, Writing – review & editing. **Wojciech Gawlik:** Validation, Funding acquisition, Writing – review & editing. **Ryszard Buczyński:** Validation, Supervision, Project administration, Funding acquisition. **Adam Wojciechowski:** Conceptualization, Investigation, Writing – review & editing. **Robert Bogdanowicz:** Funding acquisition, Formal analysis, Investigation, Writing – review & editing. **Mariusz Klimczak:** Conceptualization, Formal analysis, Writing – original draft, Writing – review & editing.

Declaration of competing interest

The authors declare that they have no known competing financial interests or personal relationships that could have appeared to influence the work reported in this paper.

Acknowledgments

The research was carried out within the TEAM NET programme of the Foundation for Polish Science co-financed by the European Union under the European Regional Development Fund, project POIR.04.04.00-00-1644/18.

Appendix A. Supplementary data

Supplementary data to this article can be found online at https://doi.org/10.1016/j.carbon.2022.04.024.

References

[1] I. Aharonovich, A.D. Greentree, S. Prawer, Diamond photonics, Nat. Photonics 5 (2011) 397–405.
[2] J.Y. Tsao, S. Chowdhury, M.A. Hollis, D. Jena, N.M. Johnson, K.A. Jones, R. J. Kaplar, S. Rajan, C.G.V. de Walle, E. Bellotti, C.L. Chua, R. Collazo, M.E. Coltrin, J.A. Cooper, K.R. Evans, S. Graham, T.A. Grotjohn, E.R. Heller, M. Higashiwaki, M. S. Islam, P.W. Juodawlkis, M.A. Khan, A.D. Koehler, J.H. Leach, U.K. Mishra, R. J. Nemanich, R.C.N. Pilawa-Podgurski, J.B. Shealy, Z. Sitar, M.J. Tadjer, A. F. Witulski, M. Wraback, J.A. Simmons, Ultrawidebandgap semiconductors: research opportunities and challenges, Adv. Electronic. Mater. 4 (2018), 1600501.
[3] J. Isberg, J. Hammersberg, E. Johansson, T. Wikström, D.J. Twitchen, A. J. Whitehead, S.E. Coe, G.A. Scarsbrook, High carrier mobility in single-crystal plasma-deposited diamond, Science 297 (5587) (2002) 1670–1672.
[4] I. Akimoto, Y. Handa, K. Fukai, N. Naka, High carrier mobility in ultrapure diamond measured by time-resolved cyclotron resonance, Appl. Phys. Lett. 105 (2014), 032102.
[5] M. Schreck, J. Asmussen, S. Shikata, J.-C. Arnault, N. Fujimori, Large-area high-quality single crystal diamond, MRS Bull. 39 (2014) 504–510.
[6] E.A. Ekimov, M.V. Kondrin, Chapter Six - high-pressure, high-temperature synthesis and doping of nanodiamonds, Semiconduct. Semimet. 103 (2020) 161–199.
[7] M.H. Alkahtani, F. Alghannam, L. Jiang, A. Almethen, A.A. Rampersaud, R. Brick, C.L. Gomes, M.O. Scully, P.R. Hemmer, Fluorescent nanodiamonds: past, present, and future, Nanophotonics 7 (8) (2018) 1423–1453.
[8] M. Rycewicz, M. Ficek, K. Gajewski, S. Kunuku, J. Karczewski, T. Gotszalk, I. Wlasny, A. Wysmołek, R. Bogdanowicz, Low-strain sensor based on the flexible boron-doped diamond-polymer structures, Carbon 173 (2021) 832–841.
[9] I.V. Fedotov, S.M. Blakley, E.E. Serebryannikov, P. Hemmer, M.O. Scully, A. M. Zheltikov, High-resolution magnetic field imaging with a nitrogen-vacancy diamond sensor integrated with a photonic-crystal fiber, Opt. Lett. 41 (3) (2016) 472–475.
[10] R.N. Patel, T. Schröder, N. Wan, L. Li, S.L. Mouradian, E.H. Chen, D.R. Englund, Efficient photon coupling from a diamond nitrogen vacancy center by integration with silica fiber, Light Sci. Appl. 5 (2016), e16032.
[11] J.-W. Fan, I. Cojocaru, J. Becker, I.V. Fedotov, M. Hassan, A. Alkahtani, A. Alajlan, S. Blakley, M. Rezaee, A. Lyamkina, Y.N. Palyanov, Y.M. Borzdov, Y.-P. Yang, A. Zheltikov, P. Hemmer, A.V. Akimov, Germanium-vacancy color center in diamond as a temperature sensor, ACS Photonics 5 (2018) 765–770.
[12] S.M. Blakley, C. Vincent, I.V. Fedotov, X. Liu, K. Sower, D. Nodurft, J. Liu, X. Liu, V. N. Agafonov, V.A. Davydov, A.V. Akimov, A.M. Zheltikov, Photonic-crystal-fiber quantum probes for high-resolution thermal imaging, Phys. Rev. Applied 13 (2020), 044048.
[13] T. Schröder, A.W. Schell, G. Kewes, T. Aichele, O. Benson, Fiber-Integrated diamond-based single photon source, Nano Lett. 11 (2011) 198–202.
[14] M. Fujiwara, O. Neitzke, T. Schröder, A.W. Schell, J. Wolters, J. Zheng, S. Mouradian, M. Almoktar, S. Takeuchi, D. Englund, O. Benson, Fiber-coupled diamond micro-waveguides toward an efficient quantum interface for spin defect centers, ACS Omega 2 (2017) 7194–7202.
[15] S. Maayani, C. Foy, D. Englund, Y. Fink, Distributed quantum fiber magnetometry, Laser Photon. Rev. 13 (2019), 1900075.
[16] H. Ebendorff-Heidepriem, Y. Ruan, H. Ji, A.D. Greentree, B.C. Gibson, T.M. Monro, Nanodiamond in tellurite glass Part I: origin of loss in nanodiamond-doped glass, Opt. Mater. Express 4 (12) (2014) 2608–2620.

[17] Y. Ruan, H. Ji, B.C. Johnson, T. Ohshima, A.D. Greentree, B.C. Gibson, T.M. Monro, H. Ebendorff-Heidepriem, Nanodiamond in tellurite glass Part II: practical nanodiamond-doped fibers, Opt. Mater. Express 5 (1) (2015) 73–87.
[18] Y. Ruan, D.A. Simpson, J. Jeske, H. Ebendorff-Heidepriem, D.W.M. Lau, H. Ji, B. C. Johnson, T. Ohshima, S. Afshar V, L. Hollenberg, A.D. Greentree, T.M. Monro, B. C. Gibson, Magnetically sensitive nanodiamond-doped tellurite glass fibers, Sci. Rep. 8 (2018) 1268.
[19] D. Bai, M.H. Huynh, D.A. Simpson, P. Reineck, S.A. Vahid, A.D. Greentree, S. Foster, H. Ebendorff-Heidepriem, B.C. Gibson, Fluorescent diamond microparticle doped glass fiber for magnetic field sensing, Apl. Mater. 8 (2020), 081102.
[20] Z. Qiao, J. Li, N. Zhao, C. Shi, P. Nash, Graphitization and microstructure transformation of nanodiamond to onion-like carbon, Scripta Mater. 54 (2) (2006) 225–229.
[21] Yu V. Butenko, V.L. Kuznetsov, E.A. Paukshtis, A.I. Stadnichenko, I.N. Mazov, S. I. Moseenkov, A.I. Boronin, S.V. Kosheev, The thermal stability of nanodiamond surface groups and onset of nanodiamond graphitization, Fullerenes, Nanotub. Carbon Nanostruct. 14 (2–3) (2006) 557–564.
[22] J. Qian, C. Pantea, J. Huang, T.W. Zerda, Y. Zhao, Graphitization of diamond powders of different sizes at high pressure–high temperature, Carbon 42 (12–13) (2004) 2691–2697.
[23] Yu V. Butenko, V.L. Kuznetsov, A.L. Chuvilin, V.N. Kolomiichuk, Kinetics of the graphitization of dispersed diamonds at "low" temperatures, J. Appl. Phys. 88 (2000) 4380.
[24] S.V. Kidalov, F.M. Shakhov, A. Ya Vul, Thermal conductivity of sintered nanodiamonds and microdiamonds, Diam. Relat. Mater. 17 (4–5) (2008) 844–847.
[25] R. Tsukahara, M. Fujiwara, Y. Sera, Y. Nishimura, Y. Sugai, C. Jentgens, Y. Teki, H. Hashimoto, S. Shikata, Removing non-size-dependent electron spin decoherence of nanodiamond quantum sensors by aerobic oxidation, ACS Appl. Nano Mater. 2 (6) (2019) 3701–3710.
[26] S. Li, D. Bai, M. Capelli, Q. Sun, S. Afshar V, D.A. Simpson, S. Foster, H. Ebendorff-Heidepriem, B.C. Gibson, A.D. Greentree, Preferential coupling of diamond NV centres in step-index fibres, Opt Express 29 (10) (2021) 14425–14437.
[27] D.R. Lide (Ed.), CRC Handbook of Chemistry and Physics, Internet Version, CRC Press, Boca Raton, FL, 2005.
[28] J. Barton, M. Gulka, J. Tarabek, Y. Mindarava, Z. Wang, J. Schimer, H. Raabova, J. Bednar, M.B. Plenio, F. Jelezko, M. Nesladek, P. Cigler, Nanoscale dynamic readout of a chemical redox process using radicals coupled with nitrogen-vacancy centers in nanodiamonds, ACS Nano 14 (10) (2020) 12938–12950.
[29] J. Shi, H. Wu, J. Liu, S. Li, X. He, Stimulated scattering effects in gold-nanorod-water samples pumped by 532 nm laser pulses, Sci. Rep. 5 (2015) 11964.
[30] V.S. Gorelik, A.F. Bunkin, M.A. Davydov, A.N. Fedorov, S.M. Pershin, A. Yu Pyatyshev, M. Wu, Forward and backward stimulated Brillouin scattering in aqueous suspension of SiO2 spherical nanoparticles, Appl. Phys. Lett. 117 (2020), 141101.
[31] J. Havlik, H. Raabova, M. Gulka, V. Petrakova, M. Krecmarova, V. Masek, P. Lousa, J. Stursa, H.-G. Boyen, M. Nesladek, P. Cigler, Benchtop fluorination of fluorescent nanodiamonds on a preparative scale: toward unusually hydrophilic bright particles, Adv. Funct. Mater. 26 (23) (2016) 4134–4142.
[32] M.D. Torelli, N.A. Nunn, O.A. Shenderova, A perspective on fluorescent nanodiamond bioimaging, Small 15 (48) (2019), 1902151.
[33] S. Stoll, A. Schweiger, EasySpin, a comprehensive software package for spectral simulation and analysis in EPR, J. Magn. Reson. 178 (2006) 42–55.
[34] A.I. Shames, V.Y. Osipov, J.P. Boudou, A.M. Panich, H.J. von Bardeleben, F. Treussart, A.Y. Vul', Magnetic resonance tracking of fluorescent nanodiamond fabrication, J. Phys. D Appl. Phys. 48 (2015), 155302.
[35] A.V. Fionov, A. Lund, W.M. Chen, N.N. Rozhkova, I.A. Buyanova, G. I. Emel'yanova, L.E. Gorlenko, E.V. Golubina, E.S. Lokteva, E. Ōsawa, V.V. Lunin, Paramagnetic centers in detonation nanodiamonds studied by CW and pulse EPR, Chem. Phys. Lett. 493 (2010) 319–322.
[36] K.V. Bogdanov, M.V. Zhukovskaya, V. Yu Osipov, E.V. Ushakova, M.A. Baranov, K. Takai, A. Rampersaud, A.V. Baranov, Highly intensive emission of the NV − centers in synthetic HPHT microdiamonds at low nitrogen doping, Apl. Mater. 6 (2018), 086104.
[37] Y. Mindarava, R. Blinder, Ch Laube, W. Knolle, B. Abel, Ch Jentgens, J. Isoya, J. Scheuer, J. Lang, I. Schwartz, B. Naydenov, F. Jelezko, Efficient conversion of nitrogen to nitrogen-vacancy centers in diamond particles with high-temperature electron irradiation, Carbon 170 (2020) 182–190.
[38] S. Kollarics, F. Simona, A. Bojtor, K. Koltai, G. Klujber, M. Szieberth, B.G. Márkus, D. Beke, K. Kamarás, A. Gali, D. Amirari, R. Berry, S. Boucher, D. Gavryushkin, G. Jeschke, J.P. Cleveland, S. Takahashi, P. Szirmai, L. Forró, E. Emmanouilidou, R. Singh, K. Holczer, Ultrahigh Nitrogen-Vacancy Center Concentration in Diamond, 2021, 02126v2 arXiv:2110.
[39] M. Seal, Graphitization of diamond, Nature 185 (1960) 522–523.
[40] S. Tulić, T. Waitz, M. Čaplovičová, G. Habler, V. Vretenár, T. Susi, V. Skákalová, Catalytic graphitization of single-crystal diamond, Carbon 185 (15) (2021) 300–313.
[41] A.M. Wojciechowski, P. Nakonieczna, M. Mrózek, K. Sycz, A. Kruk, M. Ficek, M. Głowacki, R. Bogdanowicz, W. Gawlik, Optical magnetometry based on nanodiamonds with nitrogen-vacancy color centers, Materials 12 (18) (2019) 2951.
[42] K. Beha, H. Fedder, M. Wolfer, M.C. Becker, P. Siyushev, M. Jamali, A. Batalov, C. Hinz, J. Hees, L. Kirste, H. Obloh, E. Gheeraert, B. Naydenov, I. Jakobi, F. Dolde, S. Pezzagna, D. Twittchen, M. Markham, D. Dregely, H. Giessen, J. Meijer, F. Jelezko, C.E. Nebel, R. Bratschitsch, A. Leitenstorfer, J. Wrachtrup, Diamond nanophotonics, Beilstein J. Nanotechnol. 3 (2012) 895–908.
[43] M. Alkahtani, L. Jiang, R. Brick, P. Hemmer, M. Scully, Nanometer-scale luminescent thermometry in bovine embryos, Opt. Lett. 42 (2017) 4812–4815.
[44] J.-P. Tetienne, L. Rondin, P. Spinicelli, M. Chipaux, T. Debuisschert, J.-F. Roch, V. Jacques, Magnetic-field-dependent photodynamics of single NV defects in diamond: an application to qualitative all-optical magnetic imaging, New J. Phys. 14 (2012), 103033.
[45] S. Armstrong, L.J. Rogers, R.L. McMurtrie, N.B. Manson, NV–NV electron–electron spin and NV–NS electron — electron and electron-nuclear spin interaction in diamond, Phys. Procedia 3 (2010) 1569–1575.
[46] A. Wickenbrock, H. Zheng, L. Bougas, N. Leefer, S. Afach, A. Jarmola, V.M. Acosta, D. Budker, Microwave-free magnetometry with nitrogen-vacancy centers in diamond, Appl. Phys. Lett. 109 (2016), 053505.
[47] E.R. Eisenach, J.F. Barry, L.M. Pham, R.G. Rojas, D.R. Englund, D.A. Braje, Broadband loop gap resonator for nitrogen vacancy centers in diamond, Rev. Sci. Instrum. 89 (2018), 094705.